

# Justification of the Photoplethysmography Sensor Configuration by Monte Carlo Modeling of the Pulse Waveform

Denis G. Lapitan<sup>1,\*</sup>, Andrey P. Tarasov<sup>1,2</sup>, and Dmitry A. Rogatkin<sup>1</sup>

<sup>1</sup> Moscow Regional Research and Clinical Institute ("MONIKI"), 61/2 Shchepkina str., Moscow 129110, Russia

<sup>2</sup> Federal Research Scientific Center "Crystallography and Photonics" of Russian Academy of Sciences, 59 Leninsky Avenue, Moscow 119333, Russia

\* e-mail: [lapitandenis@mail.ru](mailto:lapitandenis@mail.ru)

**Abstract.** Photoplethysmography (PPG) is an optical technique for detection of blood volume changes in the microvascular bed of a biological tissue. Many aspects of the PPG signal formation are still unclear. In particular, it is not known how the shape of a registered PPG signal depends on the geometry of tissue illumination. The aim of this study is to model the PPG waveform using the Monte Carlo (MC) method. For this, we developed a three-layer optical model of the skin in a reflectance geometry and verified it experimentally for different wavelengths (660, 810, and 940 nm) and source-detector distances (from 4 to 10 mm). The MC simulation results showed that the PPG waveform depends on the source-detector distance. The most pronounced diastolic wave is observed at the distance of 6 mm for the wavelength of 810 nm. The results obtained can be used for the development of reflectance PPG sensors. © 2022 Journal of Biomedical Photonics & Engineering.

**Keywords:** photoplethysmography; pulse waveform; model; Monte Carlo; simulation; source-detector distance.

Paper #3513 received 04 Aug 2022; accepted for publication 12 Sept 2022; published online 30 Sep 2022. [doi: 10.18287/JBPE22.08.030306](https://doi.org/10.18287/JBPE22.08.030306).

## 1 Introduction

Photoplethysmography (PPG) is a simple optical technique for detection of blood volume changes in the microvascular bed of a biological tissue [1]. The method is based on illumination of tissue with incoherent optical radiation in the visible and/or near-infrared range and recording a signal that has passed through or backscattered from the tissue [2]. The PPG signal registered consists of a variable component (AC), which is formed due to blood pulsations, and a slow varying component (DC) related to the average blood volume in a tissue [1]. Currently, PPG is actively used to assess parameters of the cardiovascular system. Clinical applications of PPG include monitoring of arterial oxygen saturation (pulse oximetry), pulse rate and its variability, cardiac output and respiration, assessment of microvascular blood flow and tissue viability, endothelial and vasomotor function, thermoregulation, etc. [1, 3]. However, morphological analysis of the pulse waveform (PW) extracted from the AC component of the PPG

signal provides other important information about the state of blood vessels, for example, their stiffness, tone, compliance, etc. [4]. Therefore, it is very important to use a correct technique for recording and processing the pulse wave signal.

As known, the pulse wave consists of direct systolic and reflected diastolic waves, as well as a dicrotic notch, which characterizes the moment of aortic valve closure [4, 5]. Herewith, the PW registered in PPG depends on many factors such as the wavelength of light illuminating the tissue, the measurement site on the body, the elasticity of vessel walls, etc. [6–8]. Many aspects of a PPG signal formation cannot be studied experimentally *in vivo*, for example, how blood volume or the concentration of different chromophores affects the signal. Hence, many researchers use methods of theoretical modeling of light propagation in tissues. One of these most used methods is the Monte Carlo (MC) approach [9, 10].

S. Chatterjee et al. investigated the effect of blood volume and oxygen saturation on optical path of light by

MC modeling applied to the pulse oximetry technique [11]. They also explored the optical parameters to PPG (pathlength, penetration depth, absorbance, reflectance and transmittance) as the functions of multiple wavelengths and source-detector separations as well as the contributions of different tissue layers and sublayers in the formation of a PPG signal [12, 13]. For this, they developed a three-dimensional comprehensive MC model of finger-PPG. Andreia V. Moço et al. developed a multilayered MC model of the skin to simulate the separate contributions from skin layers containing pulsatile arterioles to the PPG signal in the 450–1000 nm range [14]. V. Dremine et al. explored the variations in diagnostic volume due to arterial blood pulsations [15]. However, the shape of the PPG signal has not been explored in models described above. As far as we know, there are no detailed studies on how the registered PW depends on the geometry of tissue illumination, for example, on the distance between a source and a detector. This is important at the development of PPG devices based on accurate reproduction and analysis of the pulse wave signal. So, the aim of this study is the MC modeling of the photoplethysmographic PW and experimental verification of simulation results.

## 2 Materials and Methods

### 2.1 Optical Model of the Tissue

We consider the illumination of biological tissue in a reflectance geometry in which a detector is located at a distance  $r$  from a light source. When developing an optical model of the skin, we used the classical volumetric approach to simulate the PPG signal [16]. It assumes that the intensity of the signal backscattered from the tissue is modulated by changes in the medium absorption, caused, in turn, by variations in the tissue blood volume. Thus, the key parameter of the model is the blood volume. Based on this, the skin was presented as a three-layer heterogeneous medium consisting of the epidermis, dermis and deeper subcutaneous fat (see Fig. 1). The epidermis is 0.2 mm thick, the dermis is 0.7 mm thick and the subcutaneous fat is semi-infinite [17]. The dermis and subcutaneous fat of the skin are characterized by a level of blood volume  $V_b$ , which can be considered as the relative total hemoglobin fraction (Hb and HbO<sub>2</sub>) in the diagnostic volume of tissue [18].

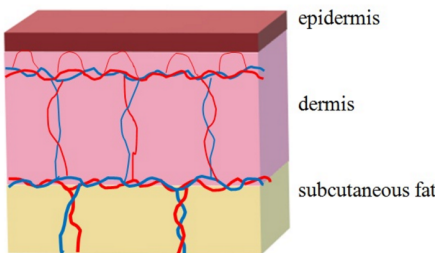


Fig. 1 Three-layer optical model of the skin.

The epidermis does not contain blood vessels and consists of connective tissue, melanin and water. Thus, we represent the absorption coefficient of the epidermal layer in the form [19]:

$$\mu_{a,epi}(\lambda) = V_{mel}\mu_{a,mel}(\lambda) + V_w\mu_{a,w}(\lambda) + [1 - (V_{mel} + V_w)]\mu_{a,baseline}(\lambda), \quad (1)$$

where  $\lambda$  is the wavelength,  $V_{mel}$  and  $V_w$  are the volume fractions of melanin and water in the epidermis, respectively,  $\mu_{a,mel}$  and  $\mu_{a,w}$  are the absorption coefficients of melanin and water,  $\mu_{a,baseline}$  is the baseline absorption coefficient, which characterizes the absorption of connective tissue in the absence of other chromophores.  $\mu_{a,baseline}$  depends on the wavelength and can be expressed by the following equation [20, 21]:

$$\mu_{a,baseline}(\lambda) = 7.84 \times 10^8 \times \lambda^{-3.255} [\text{cm}^{-1}]. \quad (2)$$

The optical properties of the dermis are highly dependent on  $V_b$ . Since the dermis, in turn, consists of different layers, such as the papillary dermis, upper blood net dermis, reticular dermis and deep blood net dermis, the level of  $V_b$  in these layers varies. It is approximately 0.04 rel. units in the papillary dermis, 0.3 rel. units in the upper blood net dermis, 0.04 rel. units in the reticular dermis and 0.1 rel. units in the deep blood net dermis [22]. Thus, the average value of  $V_b$  of the entire dermis is approximately 0.1 rel. units. We write the absorption coefficient of the dermal layer as [13, 23]:

$$\mu_{a,derm}(\lambda) = V_{b,A}\mu_{a,A}(\lambda) + V_{b,V}\mu_{a,V}(\lambda) + V_w\mu_{a,w}(\lambda) + [1 - (V_{b,A} + V_{b,V} + V_w)]\mu_{a,baseline}(\lambda), \quad (3)$$

where  $V_{b,A}$  and  $V_{b,V}$  are the volume fractions of arterial and venous blood in the dermis, respectively,  $\mu_{a,A}$  and  $\mu_{a,V}$  are the absorption coefficients of arterial and venous blood.  $\mu_{a,A}$  and  $\mu_{a,V}$ , in turn, can be expressed in terms of arterial and venous oxygen saturation  $S_a^{oxy}$  and  $S_v^{oxy}$ , respectively, as [13, 24]:

$$\begin{aligned} \mu_{a,A}(\lambda) &= S_a^{oxy}\mu_{a,HbO_2}(\lambda) + (1 - S_a^{oxy})\mu_{a,Hb}(\lambda), \\ \mu_{a,V}(\lambda) &= S_v^{oxy}\mu_{a,HbO_2}(\lambda) + (1 - S_v^{oxy})\mu_{a,Hb}(\lambda), \end{aligned} \quad (4)$$

where  $\mu_{a,HbO_2}$  and  $\mu_{a,Hb}$  are the absorption coefficients of oxygenated and deoxygenated hemoglobin.

Since the subcutaneous fat layer consists mainly of fat, we write the absorption coefficient of this layer as:

$$\mu_{a,subcut}(\lambda) = V_{b,A}\mu_{a,A}(\lambda) + V_{b,V}\mu_{a,V}(\lambda) + V_w\mu_{a,w}(\lambda) + [1 - (V_{b,A} + V_{b,V} + V_w)]\mu_{a,fat}(\lambda), \quad (5)$$

where  $\mu_{a,fat}$  is the absorption coefficient of fat.

## 2.2 Optical Properties of Skin Layers

In this study, we simulated the light propagation in the tissue by the MC approach using the developed three-layer model for the 3 wavelengths, namely: 660 nm, 810 nm and 940 nm. The absorption coefficients of melanin, oxyhemoglobin, deoxyhemoglobin, water, and fat were used from the literature [13, 19, 25–28]. When calculating the absorption coefficients of arterial and venous blood according to Eq. (4),  $S_a^{oxy}$  was set at 97% and  $S_v^{oxy}$  was set 30% lower, i.e. 67% [14]. The ratio of volume fractions of arterial and venous blood in the dermal and subcutaneous fat layers was 1:1 [13].

The scattering coefficient of each layer was determined as a combination of the Mie and Rayleigh theories in the form of an approximate dependence on the wavelength [29]:

$$\mu'_s(\lambda) = a' \left( f_{Ray} \left( \frac{\lambda}{500(nm)} \right)^4 + (1 - f_{Ray}) \left( \frac{\lambda}{500(nm)} \right)^{-b_{Mie}} \right), \quad (6)$$

where  $\mu'_s(\lambda)$  is the reduced scattering coefficient,  $a'$  is the scaling factor, which is equal to  $\mu'_s$  at the wavelength of 500 nm,  $f_{Ray}$  is the fraction of Rayleigh scattering,  $b_{Mie}$  is the power of Mie scattering. The coefficients  $a'$ ,  $f_{Ray}$  and  $b_{Mie}$  for all layers were adopted in accordance with the data of Salomatina et al. and used to calculate the scattering coefficient by Eq. (6) [29, 30]. The anisotropy

Table 1 Anatomical properties of model layers.

| Layer            | Thickness, mm | $V_{mel}$ , rel. units | $V_w$ , rel. units | $V_{b,A}$ , rel. units | $V_{b,V}$ , rel. units |
|------------------|---------------|------------------------|--------------------|------------------------|------------------------|
| Epidermis        | 0.2           | 0.1                    | 0.2                | –                      | –                      |
| Dermis           | 0.7           | –                      | 0.6                | 0.05                   | 0.05                   |
| Subcutaneous fat | $\infty$      | –                      | 0.15               | 0.025                  | 0.025                  |

Table 2 Optical properties of tissue chromophores and model layers.

| Optical parameter       | Chromophore/ Layer         | Wavelength, nm |       |      |
|-------------------------|----------------------------|----------------|-------|------|
|                         |                            | 660            | 810   | 940  |
| $\mu_a, \text{cm}^{-1}$ | Melanin                    | 269.4          | 136.2 | 83   |
|                         | Water                      | 0.0032         | 0.267 | 0.36 |
|                         | Arterial blood (Hct = 45%) | 1.95           | 4.02  | 6.43 |
|                         | Venous blood (Hct = 45%)   | 6.42           | 4.17  | 5.77 |
|                         | Fat                        | 0.65           | 1.38  | 1.44 |
| $\mu_s, \text{cm}^{-1}$ | Epidermis                  | 227.4          | 183.9 | 161  |
|                         | Dermis                     | 139.5          | 111.1 | 97.4 |
|                         | Subcutaneous fat           | 122.8          | 102.7 | 92   |

factor and the refractive index were assumed to be 0.8 and 1.4 correspondingly for all skin layers [30].

Anatomical and optical parameters of skin layers are summarized in Tables 1 and 2, respectively.

## 2.3 Modeling of the Pulse Wave Signal

It is known that the AC component of the PPG signal is formed due to arterial blood pulsations [31]. Thus, we can represent the time change in arterial blood volume as a sum of harmonic oscillations:

$$V_{b,A}(t) = V_{b0,A} + \Delta V_{b,A}(t) = V_{b0,A} \left( 1 + \sum_{k=1}^n m_k \sin(\Omega_k t) \right), \quad (7)$$

where  $V_{b0,A}$  is a some average level of arterial blood volume,  $\Delta V_{b,A}(t)$  is the variable component of arterial blood volume,  $n$  is the number of harmonics of  $V_{b,A}$  changes,  $m_k$  is the relative amplitude of the  $k^{\text{th}}$  harmonic,  $\Omega_k$  is the angular frequency of the  $k^{\text{th}}$  harmonic.  $m_k$  is defined as  $A_k/V_{b0,A}$  ( $A_k$  is the absolute amplitude of the  $k^{\text{th}}$  harmonic). Variations in  $V_{b,A}$  according to Eq. (7) lead to variations in the absorption coefficients of the dermal and subcutaneous fat layers in Eqs. (3) and (5), which, in turn, lead to amplitude modulation of the registered optical radiation in the PPG. Thus, the shape of the pulse wave can be unambiguously specified by setting the amplitudes  $m_k$  and frequencies  $\Omega_k$  in Eq. (7).

In this study, we used two harmonics to approximate the PW. The PW modeled in this way is shown in Fig. 2. The amplitudes of harmonics  $m_1 = 0.069$  and  $m_2 = m_1/1.5$  were adjusted so that the ratio of the variable component  $\Delta V_{b,A}$  to the average level  $V_{b0,A}$  was equal to 0.2 [32]. The frequencies of the first and second harmonics were set at 1 and 2 Hz, respectively.

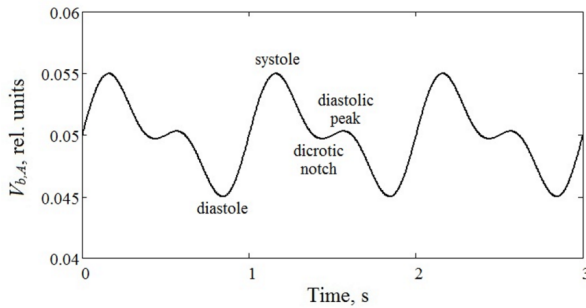


Fig. 2 Simulated time dependence of the arterial blood volume in the dermal layer, which is a pulse wave.  $V_{b0,A} = 0.05$ ,  $m_1 = 0.069$ ,  $m_2 = m_1/1.5$ ,  $\Omega_1 = 2\pi \text{ rad}$ ,  $\Omega_2 = 2 \times \Omega_1 = 4\pi \text{ rad}$ .

The main blood pulsations occur in the dermis; however, recent studies have confirmed that they are also observed in the subcutaneous fat layer, in which larger arterioles and arteries are concentrated [14]. Herewith, the magnitude of  $V_{b,A}$  oscillations in the subcutaneous fat is unknown from the literature, but it is known that it is less than in the dermis. The ratio of the  $\Delta V_{b,A}$  to the  $V_{b0,A}$  in the subcutaneous fat layer was assumed to be 8%.

## 2.4 Monte Carlo Simulation

In this study, we performed MC simulations to calculate the backscattered fluxes. The numerical model applied uses a photon weighting technique and is based on the well-known principles of MC simulation of photon transport in biological tissues [33, 34]. Disk-detector geometry was used to speed up the computation and to improve its accuracy [35]. In the simulation  $6 \times 10^7$  photon packets were launched in the medium. A round source with a diameter of 1 mm and a  $2 \times 2$  mm square detector were used. The registered flux was calculated relative to the incident flux illuminating the tissue (i.e. the relative backscattered flux) and then inverted relative to the flux at the diastole because the backscattered flux is inversely related to blood volume.

At the first stage, we calculated the backscattered fluxes at the moments of diastole and systole for all 3 wavelengths (660 nm, 810 nm and 940 nm) and for the following source-detector distances: 4, 6, 8, and 10 mm. Then, we calculated the AC/DC ratio of the PPG signal as:

$$\frac{AC}{DC} = \frac{Flux_{syst} - Flux_{diast}}{Flux_{diast}} \cdot 100\%, \quad (8)$$

where  $Flux_{syst}$  is the backscattered flux at the moment of systole,  $Flux_{diast}$  is the backscattered flux at the moment of diastole.

At the second stage, we calculated the backscattered fluxes for 4 characteristic time points of the pulse wave (diastole, systole, dicrotic notch, and diastolic peak) at the wavelength of 810 nm and for source-detector distances from 2 mm to 10 mm with a step of 2 mm. Further, we calculated the pulse waveform index (PWI) as the flux difference between diastolic peak and dicrotic notch divided by the flux difference between systole and diastole:

$$PWI = \frac{Flux_{diast\_peak} - Flux_{dicro\_notch}}{Flux_{syst} - Flux_{diast}} \cdot 100\%, \quad (9)$$

where  $Flux_{diast\_peak}$  is the backscattered flux at the diastolic peak,  $Flux_{dicro\_notch}$  is the backscattered flux at the dicrotic notch. This index characterizes the degree of expression of the diastolic peak.

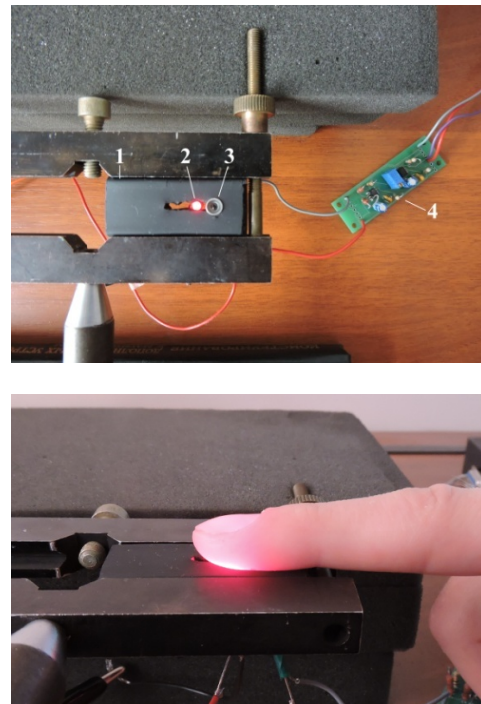


Fig. 3 Experimental setup for recording raw PPG signals from a subject's fingertip. 1 – rubber base, 2 – LED source, 3 – photodiode, 4 – signal amplification board.

## 2.5 Experimental Setup

To verify our model, we developed the experimental setup for recording raw PPG signals from a fingertip in a reflectance geometry (Fig. 3). The setup consists of a LED light source, a photodetector and a scheme of amplification and processing of the registered PPG signal. LED is controlled by the highly stable direct current source (QJ3003C III, Ningbo JiuYuan Electronic, China). The following LEDs were used as light sources: red LED (L-934SRC-C, Kingbright, China) with a peak emission wavelength of 660 nm and infrared (IR) LEDs

(IR-810-350C1, Power Light Systems, Germany; L-34F3C, Kingbright, China) with peak emission wavelengths of 810 and 940 nm, respectively. As a photodetector, a silicon photodiode (FD-10K, Russia) was used. Raw PPG signals from tissue were amplified

by AD8033 amplifier (Analog Devices, USA), digitized by 16-bit analog-to-digital converter (ADS8320EB, Texas Instruments, USA) at a sampling frequency of 320 Hz and acquired in LabView (National Instruments, USA).

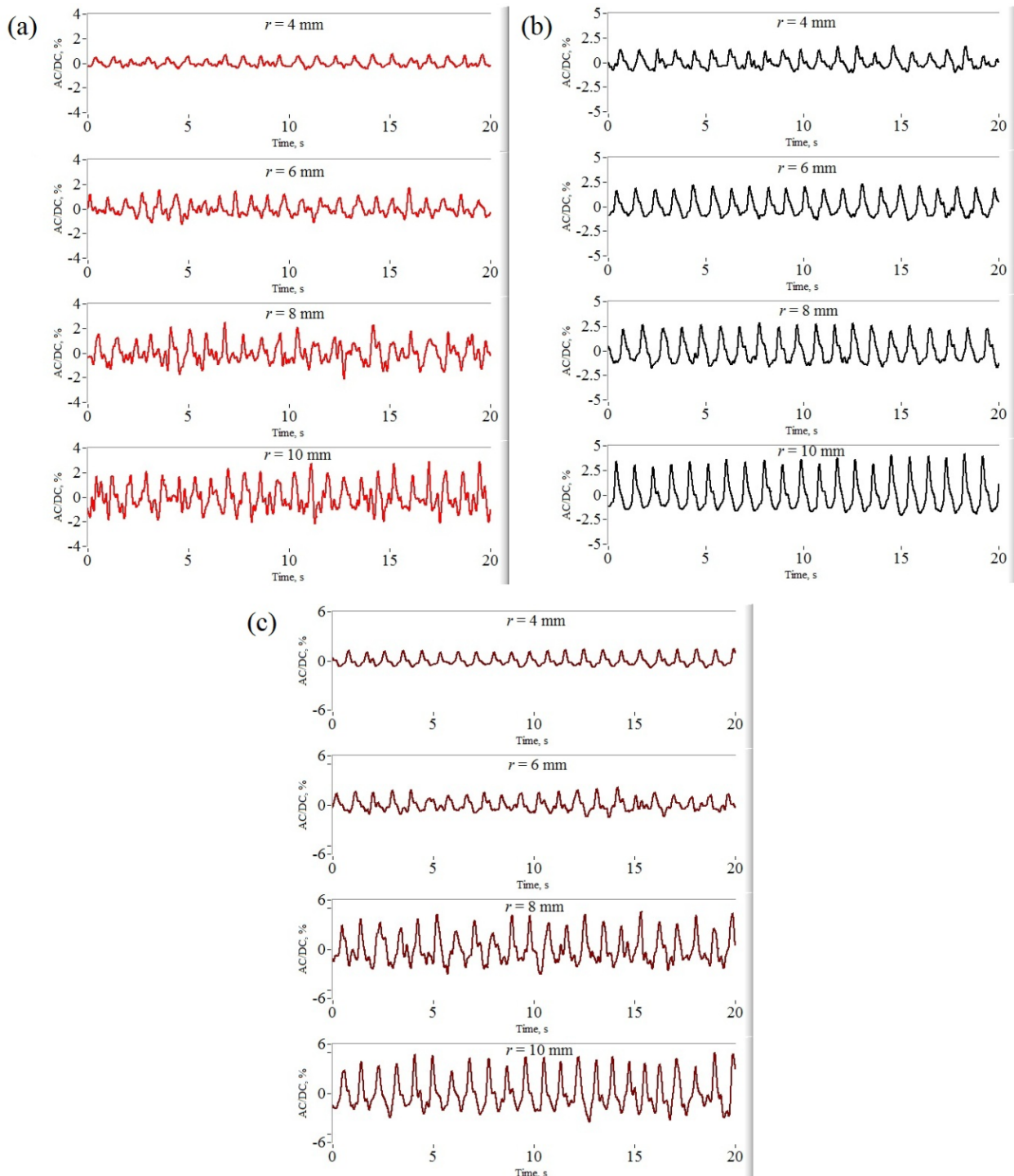


Fig. 4 An example of PPG signals, recorded from one subject for different source-detector distances (4, 6, 8, and 10 mm) at the wavelengths of 660 nm (a), 810 nm (b), and 940 nm (c).

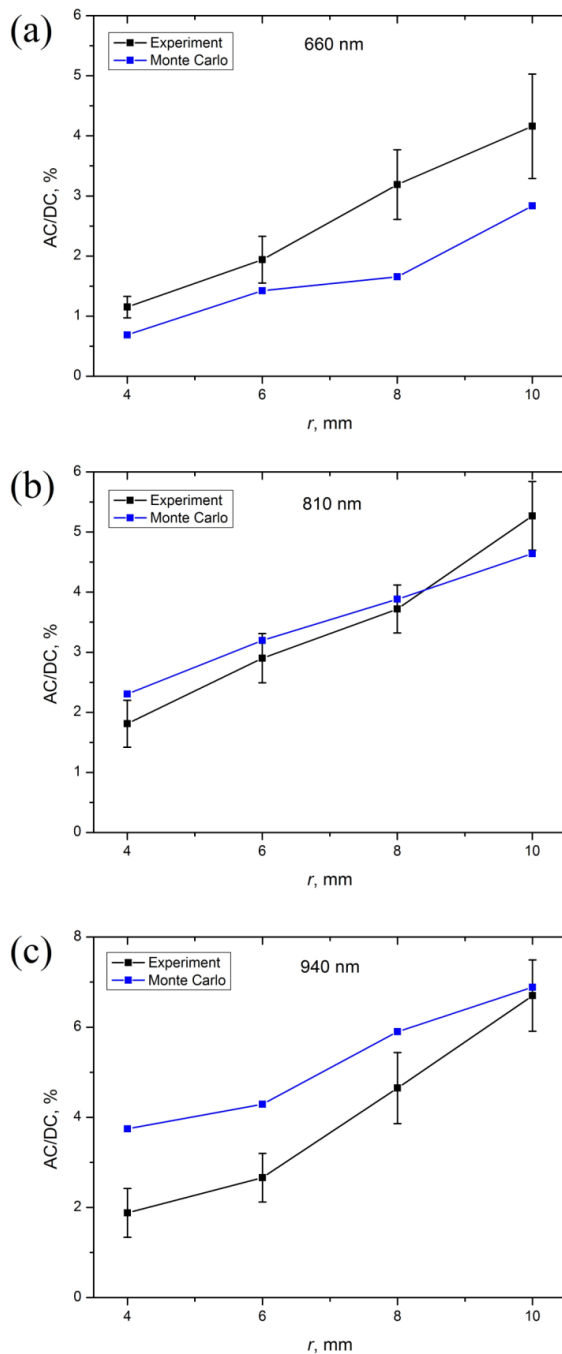


Fig. 5 The AC/DC ratio of the PPG signal for different source-detector distances obtained using MC method and from *in vivo* experiments for wavelengths of 660 nm (a), 810 nm (b), and 940 nm (c). The experimental AC/DC ratio is presented as mean  $\pm$  standard deviation.

Raw PPG signals were recorded from the fingertips of 5 healthy subjects within one minute for each wavelength (660, 810, and 940 nm) and source-detector separation (4, 6, 8, and 10 mm). Further processing of the recorded signals was performed in LabView. The PPG signals were filtered with the 3<sup>rd</sup> order Butterworth filter in the frequency range from 0.5 to 5 Hz and normalized to the DC component. The AC/DC ratio was calculated for each

pulse, averaged over all pulses in the one-minute recording and all subjects. The amplitude of the AC component was calculated as the difference between systolic and diastolic PPG signal levels.

Experimental procedures are consistent with ethical principles of the Declaration of Helsinki and were approved by the Independent Ethics Committee of Moscow Regional Research and Clinical Institute named after M. F. Vladimirov (protocol No. 13). All persons gave their informed consent prior to their inclusion in the study.

### 3 Results and Discussion

Fig. 4 illustrates the PPG signals recorded on the experimental setup for different wavelengths and source-detector distances  $r$  from one subject. The signals are presented as the ratio of the AC component to the DC one. The AC/DC PPG signal increases with increasing source-detector separation. It should be noted that the AC and DC amplitudes of the PPG signal decrease with increasing source-detector distance, which was shown by Chatterjee S. et al. [13]. However, the DC component falls faster than the AC one, thus, the AC/DC ratio increases with increasing distance, which we obtained in the experiment. As can be seen, the PW is very variable, so it is very difficult to quantify it for different source-detector distances.

The AC/DC ratio of recorded PPG signals in comparison with the one obtained using MC simulations for different wavelengths and source-detector distances is shown in Fig. 5. Since the *in vivo* PPG signal is physiologically variable, the experimental AC/DC ratios are presented as mean and standard deviation, which was calculated over the entire record and averaged for all subjects. The difference between the experimental AC/DC ratio and the theoretical one did not exceed 2% for all wavelengths. The best fit was obtained for the wavelength of 810 nm. To note, the directly proportional dependence of the AC/DC ratio on source-detector distance is not a surprise. Such behavior can be also obtained using the modified Beer-Lambert law as was shown in our previous study [36]. In general, the theoretical and experimental values of AC/DC ratio for different wavelengths are consistent with the data of other researchers [14].

Thus, the results of MC simulation have a good agreement with the experimental data, which made it possible to proceed to the next stage – PW modeling. The PPG waveform was modeled for the isobestic wavelength of 810 nm to eliminate the influence of oxygen saturation on the results. The simulated PW in the form of time dependence of  $V_{b,A}$  (see Eq. (7)) and the results for the registered flux at characteristic points of the pulse wave obtained through MC simulation for different source-detector distances are presented in Fig. 6. As can be seen, the values of the numerically calculated fluxes do not exactly follow the analytical PW. This indicates the dependence of the PW on the source-detector distance. The best match of MC fluxes to the simulated pulse wave signal was obtained for a distance of 6 mm.

The obtained dependence of the PWI on source-detector distance is presented in Fig. 7. As can be seen, the maximum of the PWI is observed at the distance of 6 mm. Thus, within our equipment configuration, this distance should be used to register the backscattered PPG signal with the most pronounced diastolic peak. It is important to note that the problem of identifying the diastolic peak from the PW is acute since many physiological indices are calculated using it, such as the reflection index, the stiffness index, the dicrotic index, etc. [5, 37]. Therefore, researchers are looking for new approaches to best distinguish the diastolic wave. In particular, Liang Y. et al. investigated various types of filters and showed that the

Chebyshev II filter of 4<sup>th</sup> order can improve the PPG signal quality more effectively than other types of filters and can be used for PPG signal processing to make the systolic and diastolic waves more salient [38]. Our results show that the diastolic wave can be more clearly identified at the stage of recording the PPG signal before filtering, if one uses an optimal distance between a source and a detector. In this study, the optimal distance is 6 mm for the wavelength of 810 nm. But this distance can also depend on the parameters of used equipment, in particular, the geometry of the light source and photodetector and the light wavelength. Further studies are needed to explore the significance of each parameter.

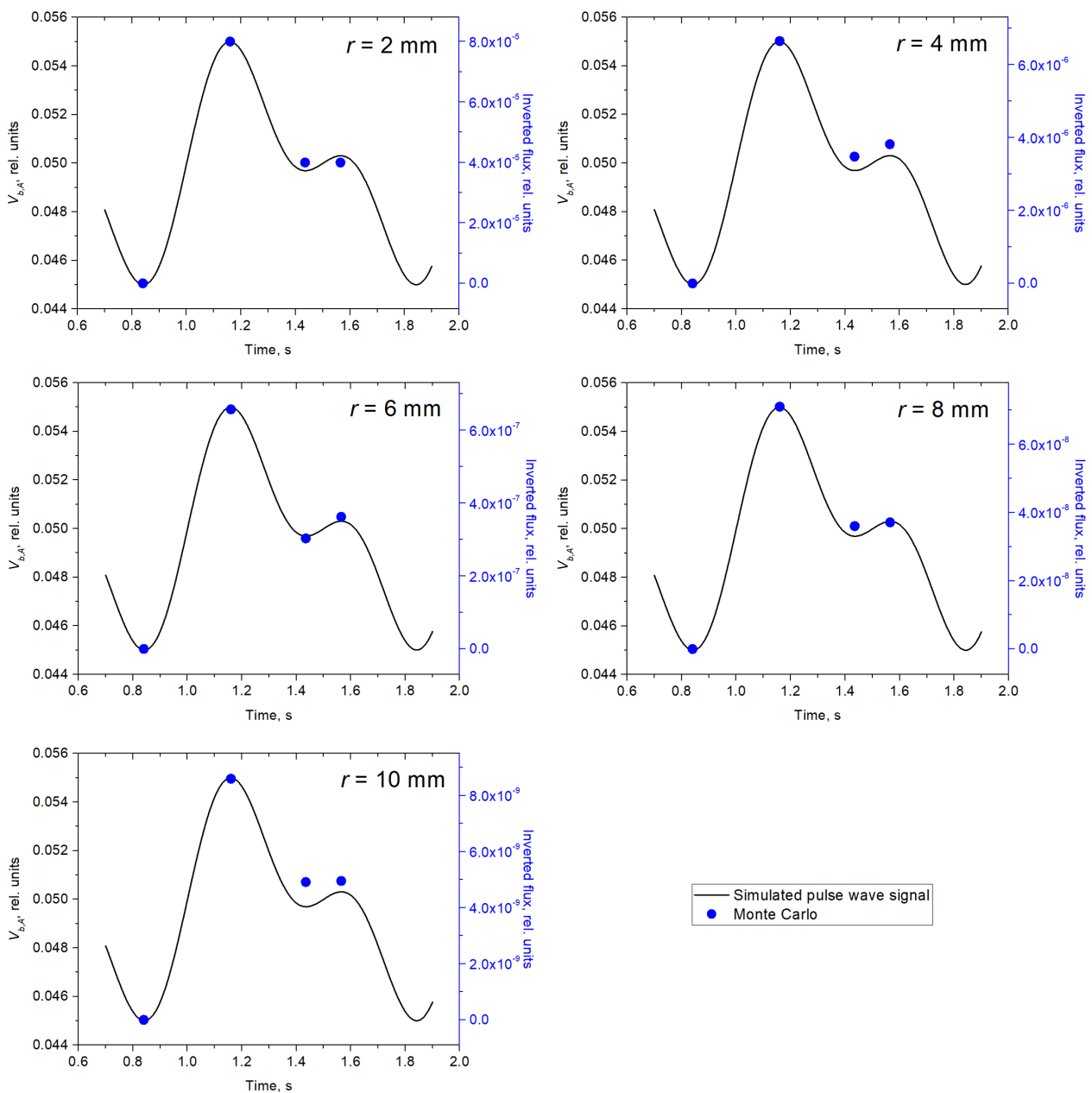


Fig. 6 The simulated PW (black line) and the fluxes at 4 time points of the pulse wave (blue dots) calculated by MC at the wavelength of 810 nm for different source-detector distances. The MC scale (right) was adjusted so that the amplitudes of the fluxes at the diastole and systole corresponded to the simulated signal.

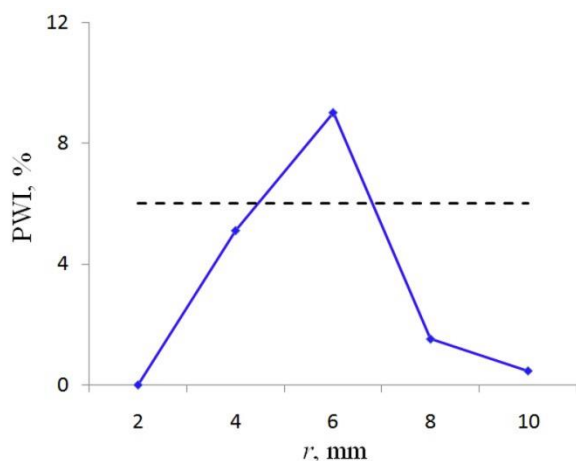


Fig. 7 The pulse waveform index (PWI) of the theoretical dependence of  $V_{b,A}$  on time (black dotted line) and flux values by MC at the wavelength of 810 nm (blue line) for different source-detector distances.

## 4 Conclusions

In this study, we proposed a three-layer reflectance model of the skin for MC simulation of the

photoplethysmographic PW. The model was verified in the experiment for different wavelengths and showed a good agreement with experimental data. Using MC simulation, the main characteristic points of the pulse wave (diastole, systole, dicrotic notch, and diastolic peak) were modeled. It was found that the PW depends on the source-detector distance. The most pronounced diastolic wave is observed at a distance of 6 mm for a wavelength of 810 nm. The results obtained can be used for a deeper understanding of the formation of a PPG signal at the development of reflectance PPG sensors.

## Disclosures

The authors declare that they have no conflict of interest.

## Acknowledgments

This work was supported by the Russian Science Foundation (project No. 21-75-00037). D. Lapitan also thanks V. Dremin (Orel State University, Russia) for his help in providing the optical properties of the tissue.

## References

1. J. Allen, "Photoplethysmography and its application in clinical physiological measurement," *Physiological Measurement* 28(3), R1–R39 (2007).
2. A. A. R. Kamal, J. B. Harness, G. Irving, and A. J. Mearns, "Skin photoplethysmography—a review," *Computer Methods and Programs in Biomedicine* 28(4), 257–269 (1989).
3. J. L. Moraes, M. X. Rocha, G. G. Vasconcelos, J. E. Vasconcelos Filho, V. H. C. De Albuquerque, and A. R. Alexandria, "Advances in photoplethysmography signal analysis for biomedical applications," *Sensors* 18(6), 1894 (2018).
4. M. Elgendi, "On the analysis of fingertip photoplethysmogram signals," *Current Cardiology Reviews* 8(1), 14–25 (2012).
5. S. C. Millasseau, J. M. Ritter, K. Takazawa, and P. J. Chowienczyk, "Contour analysis of the photoplethysmographic pulse measured at the finger," *Journal of Hypertension* 24(8), 1449–1456 (2006).
6. L. G. Lindberg, P. A. Oberg, "Photoplethysmography. Part 2. Influence of light source wavelength," *Medical & Biological Engineering & Computing* 29(1), 48–54 (1991).
7. J. Allen, A. Murray, "Age-related changes in the characteristics of the photoplethysmographic pulse shape at various body sites," *Physiological Measurement* 24(2), 297–307 (2003).
8. V. Hartmann, H. Liu, F. Chen, Q. Qiu, S. Hughes, and D. Zheng, "Quantitative comparison of photoplethysmographic waveform characteristics: effect of measurement site," *Frontiers in Physiology* 10, 198 (2019).
9. D. W. O. Rogers, "Fifty years of Monte Carlo simulations for medical physics," *Physics in Medicine & Biology* 51(13), R287 (2006);
10. V. V. Tuchin, *Tissue optics*, Society of Photo-Optical Instrumentation Engineers (SPIE), Bellingham, WA, USA (2015).
11. S. Chatterjee, J. P. Phillips, and P. A. Kyriacou, "Monte Carlo investigation of the effect of blood volume and oxygen saturation on optical path in reflectance pulse oximetry," *Biomedical Physics & Engineering Express* 2(6), 065018 (2016).
12. S. Chatterjee, P. A. Kyriacou, "Monte Carlo analysis of optical interactions in reflectance and transmittance finger photoplethysmography," *Sensors* 19(4), 789 (2019).
13. S. Chatterjee, K. Budidha, and P. A. Kyriacou, "Investigating the origin of photoplethysmography using a multiwavelength Monte Carlo model," *Physiological Measurement* 41(8), 084001 (2020).
14. A. V. Moço, S. Stuijk, and G. de Haan, "New insights into the origin of remote PPG signals in visible light and infrared," *Scientific Reports* 8(1), 8501 (2018).

15. V. Dremin, E. Zherebtsov, A. Bykov, A. Popov, A. Doronin, and I. Meglinski, “Influence of blood pulsation on diagnostic volume in pulse oximetry and photoplethysmography measurements,” *Applied Optics* 58(34), 9398–9405 (2019).
16. A. Reisner, P. A. Shaltis, D. McCombie, H. H. Asada, D. S. Warner, and M. A. Warner, “Utility of the photoplethysmogram in circulatory monitoring,” *Anesthesiology* 108(5), 950–958 (2008).
17. J. L. Reuss, “Multilayer modeling of reflectance pulse oximetry,” *IEEE Transactions on Biomedical Engineering* 52(2), 153–159 (2005).
18. A. V. Dunaev, E. A. Zherebtsov, D. A. Rogatkin, N. A. Stewart, S. G. Sokolovski, and E. U. Rafailov, “Substantiation of medical and technical requirements for noninvasive spectrophotometric diagnostic devices,” *Journal of Biomedical Optics* 18(10), 107009 (2013).
19. S. L. Jacques, “Skin optics summary,” Oregon Medical Laser Center News, January 1998 (accessed 16 May 2022). [<https://omlc.org/news/jan98/skinoptics.html>].
20. I. S. Saidi, “Transcutaneous optical measurement of hyperbilirubinemia in neonates,” PhD Thesis, Rice University, USA (1992).
21. S. L. Jacques, “Origins of tissue optical properties in the UVA, visible, and NIR regions,” *Advances in Optical Imaging and Photon Migration, Technical Digest Series, OPC364* (1996).
22. I. V. Meglinski, S. J. Matcher, “Quantitative assessment of skin layers absorption and skin reflectance spectra simulation in the visible and near-infrared spectral regions,” *Physiological Measurement* 23(4), 741–753 (2002).
23. I. V. Meglinski, S. J. Matcher, “Computer simulation of the skin reflectance spectra,” *Computer Methods and Programs in Biomedicine* 70(2), 179–186 (2003).
24. D. G. Lapitan, D. A. Rogatkin, “Variable hyperemia of biological tissue as a noise source in the input optical signal of a medical laser Doppler flowmeter,” *Journal of Optical Technology* 83(1), 36–42 (2016).
25. N. Bosschaart, G. J. Edelman, M. C. Aalders, T. G. van Leeuwen, and D. J. Faber, “A literature review and novel theoretical approach on the optical properties of whole blood,” *Lasers in Medical Science* 29(2), 453–479 (2014).
26. G. M. Hale, M. R. Querry, “Optical constants of water in the 200-nm to 200- $\mu$ m wavelength region,” *Applied Optics* 12(3), 555–563 (1973).
27. C. R. Simpson, M. Kohl, M. Essenpreis, and M. Cope, “Near-infrared optical properties of ex vivo human skin and subcutaneous tissues measured using the Monte Carlo inversion technique,” *Physics in Medicine & Biology* 43(9), 2465–2478 (1998).
28. A. N. Bashkatov, E. A. Genina, and V. V. Tuchin, “Optical properties of skin, subcutaneous, and muscle tissues: a review,” *Journal of Innovative Optical Health Sciences* 4(1), 9–38 (2011).
29. S. L. Jacques, “Optical properties of biological tissues: a review,” *Physics in Medicine & Biology* 58, R37–R61 (2013).
30. E. Salomatina, B. Jiang, J. Novak, and A. N. Yaroslavsky, “Optical properties of normal and cancerous human skin in the visible and near-infrared spectral range,” *Journal of Biomedical Optics* 11(6), 064026 (2006).
31. J. Allen, C. P. Oates, T. A. Lees, and A. Murray, “Photoplethysmography detection of lower limb peripheral arterial occlusive disease: a comparison of pulse timing, amplitude and shape characteristics,” *Physiological Measurement* 26(5), 811–821 (2005).
32. J. M. Schmitt, G. X. Zhou, E. C. Walker, and R. T. Wall, “Multilayer model of photon diffusion in skin,” *Journal of the Optical Society of America A* 7(11), 2141–2153 (1990).
33. S. A. Prahl, M. Keijzer, S. L. Jacques, and A. J. Welch, “A Monte Carlo model of light propagation in tissue,” *SPIE Proceedings* 10305, 1030509 (1989).
34. L. Wang, S. L. Jacques, and L. Zheng, “MCML—Monte Carlo modeling of light transport in multi-layered tissues,” *Computer Methods and Programs in Biomedicine* 47(2), 131–146 (1995).
35. A. P. Tarasov, “Acceleration of Monte Carlo simulation of light transport in tissues using disk-detector geometry in the backscattering problem,” in 2020 International Conference Laser Optics (ICLO), 2–6 November 2020, Saint Petersburg, Russia (2020).
36. D. G. Lapitan, A. P. Tarasov, “Analytical assessment of the modulation depth of photoplethysmographic signal based on the modified Beer-Lambert law,” in 2019 IEEE 8th International Conference on Advanced Optoelectronics and Lasers (CAOL), 6–8 September 2019, Sozopol, Bulgaria, 103–106 (2019).
37. E. von Wowern, G. Östling, P. M. Nilsson, and P. Olofsson, “Digital photoplethysmography for assessment of arterial stiffness: repeatability and comparison with applanation tonometry,” *PLoS ONE* 10(8), e0135659 (2015).
38. Y. Liang, M. Elgendi, Z. Chen, and R. Ward, “An optimal filter for short photoplethysmogram signals,” *Scientific Data* 5(1), 180076 (2018).